nature communications

Article

https://doi.org/10.1038/s41467-025-61005-8

The human ciliopathy protein RSG1 links the CPLANE complex to transition zone architecture

Received: 23 September 2024

Accepted: 10 June 2025

Published online: 01 July 2025

Check for updates

Neftalí Vazquez[1,12], Chanjae Lee[1,12], Irene Valenzuela[2,12], Thao P. Phan[3], Camille Derderian[3], Marcelo Chávez[4], Nancie A. Mooney[4], Janos Demeter[4], Mohammad Ovais Aziz-Zanjani[4], Ivon Cusco[2], Marta Codina[2], Núria Martínez-Gil[2], Diana Valverde[5], Carlos Solarat[5], Ange-Line Buel[6], Cristel Thauvin-Robinet[6], Elisabeth Steichen[7], Isabel Filges[8], Pascal Joset[8], Julie De Geyter[8], Krishna Vaidyanathan[1], Tynan P. Gardner[1], Michinori Toriyama[9], Edward M. Marcotte[1], Kevin Drew[10], Elle C. Roberson[11], Peter K. Jackson[4], Jeremy F. Reiter[3], Eduardo F. Tizzano[2,12] ✉ & John B. Wallingford[1,12] ✉

Cilia are essential organelles, and variants in genes governing ciliary function result in ciliopathic diseases. The Ciliogenesis and PLANar polarity Effectors (CPLANE) protein complex is essential for ciliogenesis, and all but one subunit of the CPLANE complex have been implicated in human ciliopathy. Here, we identify three families in which variants in the remaining CPLANE subunit *CPLANE2/RSG1* also cause ciliopathy. These patients display cleft palate, tongue lobulations and polydactyly, phenotypes characteristic of Oral-Facial-Digital Syndrome. We further show that these alleles disrupt two vital steps of ciliogenesis, basal body docking and recruitment of intraflagellar transport proteins. Moreover, APMS reveals that Rsg1 binds CPLANE and the transition zone protein Fam92 in a GTP-dependent manner. Finally, we show that CPLANE is generally required for normal transition zone architecture. Our work demonstrates that *CPLANE2/RSG1* is a causative gene for human ciliopathy and also sheds new light on the mechanisms of ciliary transition zone assembly.

Ciliopathies are a broad class of human diseases that share an etiology of defective cilia structure or function. These diseases span skeletal anomalies, craniofacial defects, cystic kidneys, blindness, obesity and other clinical manifestations, highlighting the wide array of physiological functions that require components of the cilium[1–3]. Cilia are assembled and maintained by a cohort of multiprotein machines, such as the IFT complexes[4,5], the BBSome[6], transition zone complexes[7], and variants in subunits of these complexes are sufficient to cause ciliopathies[2,3]. The Ciliogenesis and PLANar polarity Effector (CPLANE) complex is also essential for ciliogenesis in all vertebrates including humans[8], yet its function remains far less well defined.

Identified initially as a tripartite complex that controls planar cell polarity in *Drosophila*, the vertebrate CPLANE complex comprises five proteins[8]. Fuz/Cplane3 and Intu/Cplane4 were the first vertebrate orthologues to be described; in *Xenopus* they are essential for ciliogenesis by dint of their roles in basal body docking and recruitment of IFT-A2 proteins to the base of cilia[9–12]. More recently, it was shown that Fuz and Intu together form a GEF for Rab23, which in turn is implicated in the docking of basal bodies to the apical surface[13–15].

Rsg1/Cplane2 was identified as a Fuz-interacting small GTPase essential for ciliogenesis in *Xenopus*[12,16]. Wdpcp/Cplane5 encodes a beta-propeller protein and was first found to be essential for

A full list of affiliations appears at the end of the paper. ✉e-mail: eduardo.tizzano@vallhebron.cat; wallingford@utexas.edu

ciliogenesis in *Xenopus*[17]. Further studies revealed that each of these CPLANE subunits is essential for ciliogenesis in mice[16,18–21], with Rsg1 acting at a relatively late step in ciliogenesis[22].

Proteomic analysis revealed that Intu, Fuz, Wdpcp, and Rsg1 form a stable and discrete complex that also contains the human ciliopathy protein Jbts17/CPLANE1[23]. Recently, the structure of a partial CPLANE complex lacking Jbts17 was solved by CryoEM (Fig. 1A) revealing a similar structure to other hexa-longin domain GEFs such as Mon1-Czz1 and Hps1-Hps4, and that Fuz interacts directly with Rsg1[15]. This structure suggests Rsg1 is not a substrate of the Intu/Fuz GEF, but rather an effector[15]. Studies in a variety of cell types indicate that the CPLANE complex localizes near basal bodies, where it assembles hierarchically, with Rsg1 being the most downstream component[22,23].

Finally, pathogenic variants in all but one CPLANE subunit have now been shown to be causative for human ciliopathy[17,23–30]. These variants disrupt both lipid binding by the CPLANE complex and IFT-A2 recruitment to basal bodies[15,23]. Though disruption of basal body docking is a common feature of CPLANE disruption in *Xenopus*[10,12], it remains unknown if ciliopathic variants in human *CPLANE* genes affect basal body docking. Unlike all other CPLANE genes, *CPLANE2/RSG1* has yet to be linked to human disease.

Here, we identified three families in which homozygous or compound heterozygous variants in *CPLANE2/RSG1* correlate with a ciliopathy phenotype within the spectrum of Oral-Facial-Digital syndrome (OFD). More precisely, the phenotype was quite similar to that reported for another of the ciliopathies related to the CPLANE complex (*CPLANE1*[24]). Using in vivo imaging, we show that these alleles disrupt not only IFT-A2 recruitment but also basal body docking. One of these alleles lies within the GTP-binding domain of Rsg1, and proteomic analysis revealed that Rsg1 interaction with all CPLANE subunits is GTP-dependent. We also discovered a GTP-dependent interaction of Rsg1 and the BAR domain ciliopathy protein Fam92a. Based on that insight, we identified an unexpected role for Rsg1 and the CPLANE complex in maintaining the normal architecture of the ciliary transition zone. Together, these results shed new light on the mechanisms of CPLANE action during ciliogenesis and how it is disrupted in CPLANE-associated ciliopathy.

Results

Allelic variants of *CPLANE2/RSG1* cause human ciliopathy

We identified two patients in which variants in *CPLANE2* segregated with a spectrum of anomalies resembling OFD. The first patient presented with polyhydramnios during gestation, bilateral pre-and post-axial polydactyly on hands and feet, hypertelorism, high arched palate, and tongue lobulation (Fig. 1B; Supplementary Clinical Report; Supplementary Dataset. 1, 2). This patient was previously described, but no molecular explanation was identified at that time[31]. Exome sequencing identified compound heterozygous variants in *CPLANE2*. The maternally inherited variant (NM_030907.4:c.226 G > C/c.−25C > G) lies in the coding region and changes Ala76 to Pro, the impact of which is described below. The paternal allele (NM_030907.4:c.−25C > G) lies in the 5′ untranslated region. Analysis using RiboNN[32] predicts this allele will cause a modest but significant reduction in translation efficiency and thus affect RSG1 protein levels. (Note: To accommodate changing nomenclature, this paper will use the current formal human gene names (*CPLANE2*, etc.), but will use the names of protein subunits that are consistent with previously published literature (Rsg1, etc.).

The second patient had prenatal detection of aortic coarctation and presented with a normal palate but a lobulated tongue and laryngomalacia, as well as a cardiac septal defect and post-axial polydactyly in one hand and pre-axial polydactyly on both feet. Exome sequencing for this patient identified a homozygous variant (NM_030907:c.G353A) in the coding region changing Gly118 to Glu (Fig. 1D; Supplementary Fig. 1; Supplementary Clinical Report; Supplementary Datasets 1, 2).

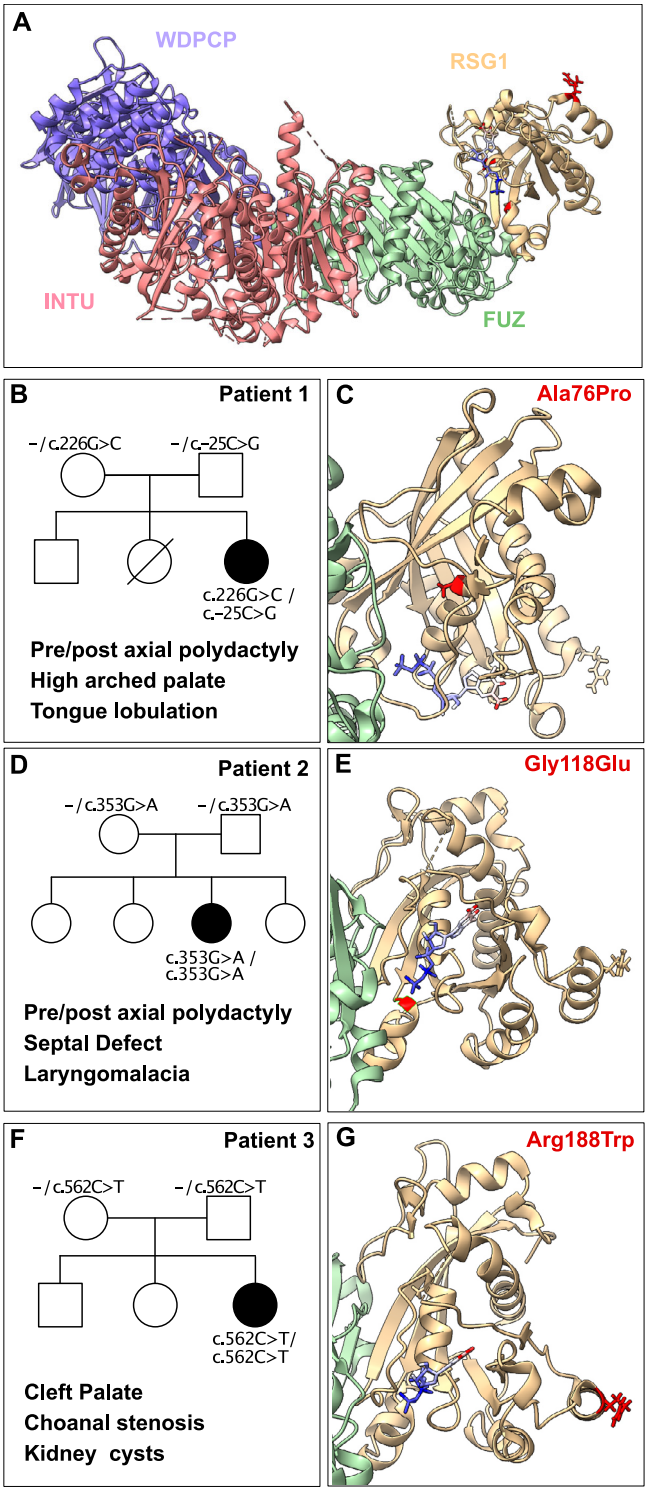

Fig. 1 | Allelic variants of *RSG1/CPLANE2* are associated with human ciliopathy. **A** Structure of mouse CPLANE complex, Wdpcp, Intu, Fuz, and Rsg1 (PDB: 7Q3E). *RSG1* allelic variants highlighted in red and GTP in the nucleotide pocket indicated (**B**, **D**, **F**) Pedigree maps and prominent features for ciliopathy indicated patients. (**C**, **E**, **G**) Structure of mouse Rsg1 (PDB 7q3e) with corresponding human residues altered by ciliopathy variants highlighted in red (see also Supplementary Fig. 2B, C).

Finally, in the third patient, we observed a somewhat milder phenotype, but also consistent with the clinical manifestations of the ciliopathy spectrum. During pregnancy, ultrasound identified hypoplastic and cystic dysplastic kidneys, oligohydramnios, microcephaly, and IUGR. After birth the patient displayed no polydactyly, but

presented with a cleft palate, choanal stenosis, pulmonary hypoplasia, and kidney cysts. In this patient, exome sequencing identified a homozygous variant (NM_030907:c.562 C > T) that results in an Arg188 to Trp change in the coding region (Fig. 1F; Supplementary Clinical Report; Supplementary Dataset 1,2).

Because polydactyly and defects in the palate, tongue, larynx, and kidneys are hallmarks of CPLANE disruption in mice[16,18–20,22,23,33], these data raise the possibility that these variants in *CPLANE2/RSG1* are causative for the ciliopathy phenotype in these patients.

RSG1 variants disrupt RSG1 function via distinct mechanisms

To understand the molecular etiology of ciliopathic *CPLANE2* alleles, we first mapped their position to the known structure of RSG1[15], which is generally similar to that of Rab GTPases (Supplementary Fig. 2). AlphaFold3[34] predicts human RSG1 to fold in a manner very similar to the known structure of mouse Rsg1, characterized by a central β-sheet surrounded by five α-helices (Supplementary Fig. 2B, C).

The alanine at human position 76 anchors the α1 helix; this residue differs among vertebrates but is strongly conserved for small amino acids (Fig. 1C; Supplementary Fig. 2A, C). For example, Ser is substituted in *Xenopus* while other amphibians and reptiles have Gly and Val in this position (e.g., see Uniprot A0A6P8NQI1 and A0AA97KFT7, respectively). Importantly, AlphaFold Missense[35] predicts all of these substitutions to be benign, and structurally speaking, any of these small amino acids would be compatible with the alpha helical region in which the residue lies. By contrast, the proline at this position in our patient would be predicted to disrupt the alpha helix and thus the global tertiary fold. Accordingly, AlphaFold Missense predicts a proline at this position to be deleterious[35].

The G118 is conserved in *Xenopus* (=G114) (Supplementary Fig. 3) and lies within the G3 region of the GTP binding pocket, immediately adjacent to the a key residue predicted to mediate GTP binding of Rsg1, E119[15] (Fig. 1E; Supplementary Fig. 2A, C). Nearly any mutation at this position is predicted by AlphaMissense to be pathogenic[35], which is likely for two reasons. First, glycine backbone torsion angles are more conformationally flexible than all other residues. The backbone conformation at position 118 occupies a region of Ramachandran space that is energetically unfavorable for any other amino acid ($\varphi = 98.6$, $\psi = 146.1$, measured with PyMOL's measurement tool). Second, the location of position 118 is tightly packed by other amino acid side chains, and any amino acids with large side chains would likely disrupt the interaction with the adjacent GTP.

R188 lies on the outside edge of the a4 helix, away from the GTP-binding region and away from the known sites of Rsg1 interaction with Fuz (Fig. 1G, Supplementary Fig. 2A, C). This arginine at human residue 188 is not well conserved and is changed to aspartic acid in *Xenopus* (Supplementary Fig. 3), but importantly, this change is conservative; both residues are polar and either could make energetically favorable interaction with solvent. Indeed, AlphaFold Missense predicts the change between human and frog to be benign[35]. By contrast, the patient-associated change to the non-polar tryptophan would likely disrupt any hydrogen bond network at a protein interaction interface and expose a large hydrophobic group (i.e. Trp) to bulk solvent resulting in a thermodynamic penalty.

To directly explore pathogenicity, we tested these alleles' effect on localization of Rsg1 protein using multiciliated cells (MCCs) in *Xenopus* (Fig. 2A), a proven platform for modeling the cell biology of ciliopathies[36,37]. Because protein/protein interactions co-evolve, we used equivalent variants in the *Xenopus* orthologue of Rsg1 for these experiments (Supplementary Fig. 3).

As expected[16], we found that wild-type Rsg1 localized strongly to basal bodies (BB's) (Fig. 2B). In contrast, *Xenopus* S72P (=human A76P) displayed significantly reduced enrichment at basal bodies (Fig. 2C). We quantified the alleles reduced recruitment to BBs as the ratio of Rsg1-GFP to Centrin-RFP (Fig. 2F). We noted as well that the S72P allele appeared poorly expressed (Fig. 2C, F), and western blots confirmed significantly reduced Rsg1^{S72P}-GFP compared to Rsg1-GFP protein (Supplementary Fig. 4). G114E (=human G118E) was significantly reduced from basal bodies as compared to control (Fig. 2D, F), though expression was robust in western blots (Supplementary Fig. 4).

Finally, we found that *Xenopus* D184W (=human R188W) displayed essentially normal recruitment to basal bodies (Fig. 2E, F) and also generated normal levels of protein in western blots (Supplementary Fig. 4). The normal BB localization is consistent with the fact that while interaction with other CPLANE subunits is required for BB recruitment of Rsg1[23], the R188/D184 residue lies on the external surface of Rsg1. We therefore sought to further test the impact of these ciliopathy alleles in vivo.

RSG1 variants disrupt IFT-A2 recruitment to basal bodies

CPLANE is implicated in the recruitment of IFT-A2 to basal bodies and ciliopathy-associated alleles of *JBTS17* and *INTU* disrupt this function[11,12,23]. As a direct test of pathogenicity, we asked if suspected ciliopathy alleles of *CPLANE2/RSG1* did likewise. First, we confirmed that Rsg1 knockdown (KD) disrupted BB recruitment of the IFT-A2 subunit Ift43[12], and that this defect was significantly rescued by co-expression of wild-type Rsg1 (Fig. 3A–C, G). Consistent with the absence of a stable protein, co-expression of S72P did not significantly increase recruitment of Ift43-GFP over the knockdown (Fig. 3D, G). Likewise, and consistent with the failure of G114E to localize to BB's, expression of this allele also failed to significantly increase Ift43 levels above the knockdown (Fig. 3E, G).

Interestingly, Ift43 levels after D184W expression were significantly below control levels and below the levels of WT Rsg1 rescue but displayed a modest but significant increase when compared to knockdown (Fig. 3F, G). These levels were also significantly increased compared to either S72P or G114E. Consistent with the more conservative predicted effect on protein structure (Fig. 1), these data suggest that D184W is by comparison a quantitatively milder variant. Thus, we conclude that all three ciliopathy alleles of *RSG1* are at least somewhat pathogenic due their failure to mediate IFT-A2 recruitment to basal bodies.

RSG1 and *JBTS17* variants disrupt basal body docking

Loss of CPLANE subunits causes basal body docking defects in *Xenopus* and mice[10,12,22], but whether disruption of basal body docking contributes to CPLANE-associated ciliopathy remains unknown. We therefore asked if ciliopathy variants of *CPLANE2* impact basal body docking in *Xenopus* MCCs (Fig. 4A). To this end, we first confirmed that Rsg1 KD disrupted BB docking[12] and that this defect could be significantly rescued by co-expression of wild-type Rsg1 (Fig. 4B–D, H). As expected, S72P failed to rescue BB docking; mean BB depth after expression of this allele was not significantly different from knockdown (Fig. 4E, H). Interestingly, however, G114E did rescue docking with modest significance, and notably, D184W elicited a highly significant rescue of BB depth compared to knockdown (Fig. 4F–H). However, these rescues fell well short of normal, with BB depths remaining significantly different from controls and from rescue with WT Rsg1.

These results prompted us to ask if pathogenic variants in other CPLANE subunits may also act in part via BB docking. We found that knockdown of Jbts17 elicited severe basal body docking defects in *Xenopus* MCCs, and these could be effectively rescued by co-expression of wild-type Jbts17-GFP (Supplementary Fig. 5B–D, F). By contrast, expression of the ciliopathy-associated truncation Jbts17-Arg1569*[38] failed to rescue BB docking (Supplementary Fig. 5E, F).

GTP binding is required for Rsg1 association with CPLANE

Having found that pathogenic variants in *CPLANE2* cause human ciliopathy, we sought a deeper understanding of the encoded protein's

https://doi.org/10.1038/s41467-025-61005-8

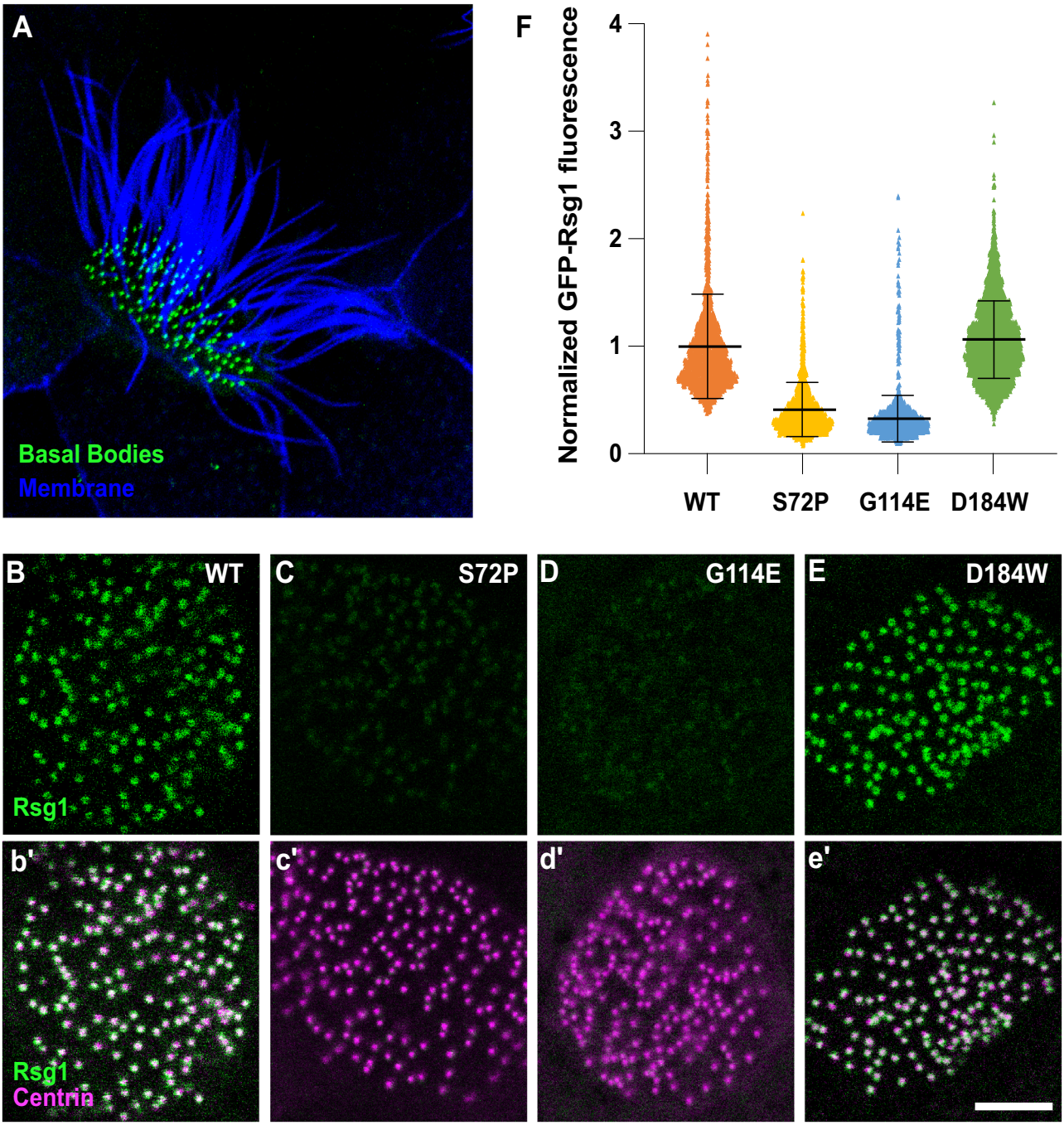

Fig. 2 | Ciliopathy-associated alleles of *RSG1* elicit distinct effects. A En face in vivo imaging of a *Xenopus* multiciliated cell with axonemes labelled by membrane-RFP (blue) and basal bodies labeled with centrin-BFP (green). **B**–**E** En face images of single MCCs showing Rsg1 basal body localization for control, and S72P (=human A76P), G114E (=human G118E), and D184W (=human R188W) variants. (**b'**–**e'**) merged channels showing Rsg1(green) with centrin (magenta), scale bar = 5 µm. **F** Graph showing mean ± standard deviation of normalized GFP-Rsg1 basal body fluorescence (see "Methods"). *N* > 25 cells in 5 embryos across 3 experiments for all conditions. *N* values and statistic can be found in Supplementary Dataset 3.

molecular functions. *RSG1* encodes a small GTPase. It binds GTP in vitro[15] and we previously showed that the canonical T→N mutation in the GTP-binding pocket disrupts basal body localization and disrupts basal body docking and IFT-A2 recruitment activity in vivo[16]. But while the pathogenic G118E allele lies squarely within the GTP binding pocket (Fig. 1E), the molecular consequences of GTP binding by Rsg1 have never been explored.

We therefore expressed wild-type Rsg1 or GDP-locked Rsg1^{T69N} in ciliated mouse IMCD3 cells and used affinity purification and mass spectrometry (APMS) to compare their interactomes. Analysis of Rsg1 peptides revealed that the two proteins were equivalently expressed and recovered in APMS (Supplementary Dataset 5), and consistent with previous studies[15,23], APMS with wild-type Rsg1 strongly enriched all known CPLANE components, including not only Fuz, Intu, and Wdpcp, but also Jbts17 (Fig. 5; Supplementary Dataset 3)(Data deposited in PRIDE: Project accession: PXD055830). Strikingly, interactions with all four CPLANE subunits were almost completely absent for Rsg1^{T69N} (Fig. 5; Supplementary Dataset 3), suggesting the interactions are GTP-dependent. This result strongly suggests that GTP loading of Rsg1 is essential for its function and that other relevant interaction

https://doi.org/10.1038/s41467-025-61005-8

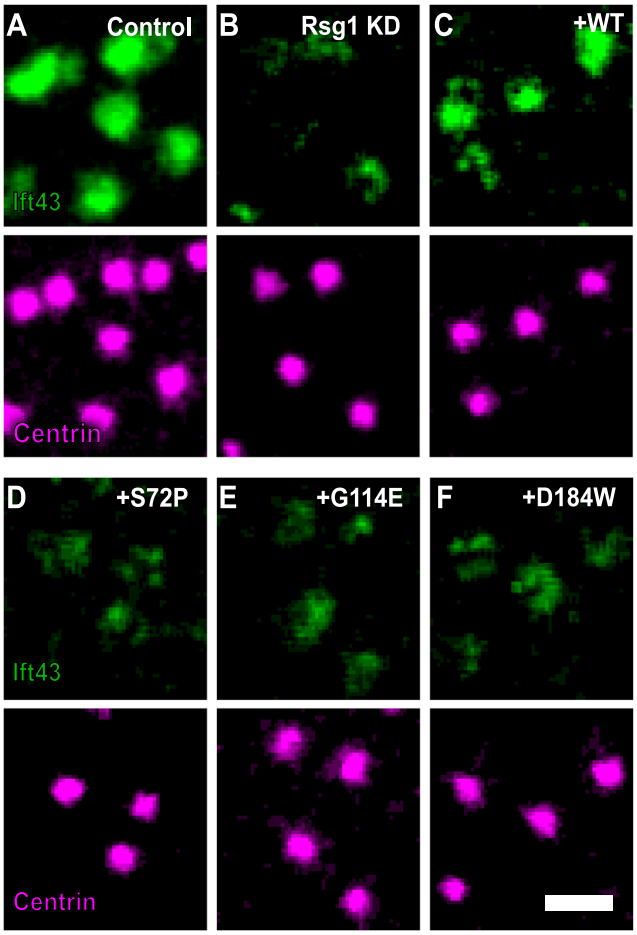

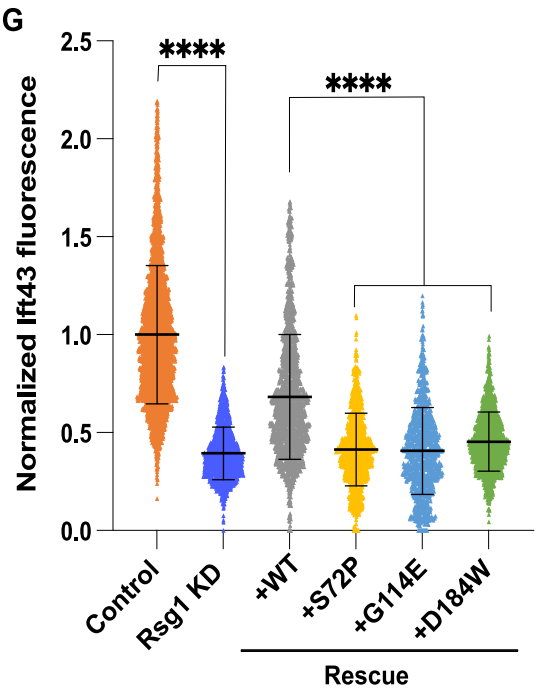

Fig. 3 | Ciliopathy-associated alleles of *RSG1* disrupt IFT-A2 recruitment to the base of cilia. A–F High magnification *en face* images showing IFT43 (green) localization at apical basal bodies labeled by centrin (magenta). **A–C** Control, Rsg1 KD, and rescue of KD with WT Rsg1. **D–F** Failure of rescue by indicated variant alleles. Scale bar= 1 µm. **G** Graph showing mean ± standard deviation of normalized IFT43-GFP basal body fluorescence. *N* > 21 cells in 6 embryos across 2 experiments for all conditions. *N* values and statistics can be found in Supplementary Dataset 3.

partners might also be identified by their specific failure to interact with Rsg1^{T69N}. We therefore examined our interactomes for further insight into Rsg1 function.

The GTP-dependent Rsg1 interactome

Because Intu and Fuz form a hexa-longin GEF[13–15], it is interesting that apart from other CPLANE subunits, the most robustly enriched protein in our APMS was Hps1 (Fig. 5; Supplementary Dataset 4), a subunit of the BLOC3 hexa-longin GEF complex[39]. Also enriched was Rab5c (Fig. 5; Supplementary Dataset 4), which is a known substrate of yet another hexa-longin GEF, Mon1-Ccz1-Bulli[40]. These interactions warrant further investigation, as they raise the possibility of promiscuity, not just among effectors and substrates, but also among subunits of hexa-longin domain GEFs. In addition, several other Rabs were enriched specifically by wild-type Rsg1 but not Rsg1^{T69N}, including Rab3B and the ciliogenic Rab29[41] (Fig. 5; Supplementary Dataset 4).

CPLANE subunits have also been implicated in actin assembly[9,42,43]. It was interesting, then, that several actin-binding proteins were enriched specifically by wild-type Rsg1 but not Rsg1^{T69N}. The most interesting were Pfn1 and Pdlim4, which are both dysregulated in a mouse model of retinal ciliopathy[44], and Coro1C, which is present in the ciliary membrane proteome[45] (Fig. 5; Supplementary Dataset 4).

Finally, we found GTP-dependent interaction between Rsg1 and three proteins related to the ciliary transition zone, Fam92a/Cibar1, Cby1, and Dzip1 (Fig. 5; Supplementary Dataset 4). These three proteins interact with one another, are essential for ciliogenesis, and are implicated in human ciliopathy[46–51]. Because the CPLANE proteins have not been associated previously with the ciliary transition zone, we explored these interactions further.

AlphaFold predicts direct RSG1/FAM92A interaction

To understand the nature of the RSG1 interaction with TZ proteins, we used AlphaFold3 (AFold3) to explore its structural basis[34]. Only FAM92A was predicted to interact directly with RSG1 (Fig. 6), though there are known interactions among FAM92A, CBY1, and DZIP1[47,49,52]. We used co-IP with in vitro translated proteins to confirm direct interaction of *Xenopus* Fam92a and Rsg1 (Supplementary Fig. 6A).

Fam92a is a BAR domain protein that exists predominantly in a dimeric form[53] and Rsg1 forms a stable complex with Fuz[15], so we modeled a FAM92A homodimer with two RSG1/FUZ heterodimers (Fig. 6B, C). The FAM92A BAR domains formed a strongly predicted curved dimer with one RSG1/FUZ dimer predicted to bind at each end (Fig. 6B, C). This structure was consistently predicted across multiple seeds with Afold3 and also predicted by AFold2 multimer[54] (Supplementary Fig. 6B, C).

We performed several additional tests of the veracity of this prediction. First, we modeled interaction of monomers of RSG1 and FAM92A, and the Predicted Aligned Error (PAE) suggested that the structure of each monomer was confidently modeled, as was the interface of the key C-terminal helix of FAM92 with RSG1 (Fig. 7A, dotted box). The interface predicted template modeling (ipTM) score for the overall model was 0.78 and the predicted local distance difference test (pLDDT) score for the C-terminal helix of FAM92A that contacts RSG1 was >70 (Fig. 6B). Even stronger scores were found when we modeled an RSG1 monomer with only the C-terminus of FAM92A (Fig. 7C, D). By contrast, no interaction was predicted when queried with RSG1 and FAM92A lacking the C-terminus (Fig. 6E, F).

This overall structure of Fam92 interaction with Rsg1 calls to mind the paired dimer structure of Rab GTPases bound to their effectors, such as Rab10 and Mical1 or Rab11b and FIP2[55]. Moreover, the combined involvement of the N-terminus, the α3-β5 loop, and the C-terminal region of the α5 helix of Rsg1 to interact with the C-terminal helixes of FAM92A (Fig. 6C, D; Supplementary Fig. 2) bears at least some similarity to the mechanism revealed by crystallography for interaction of Rab3a with the C-terminus of its effector Rabphilin3[56].

https://doi.org/10.1038/s41467-025-61005-8

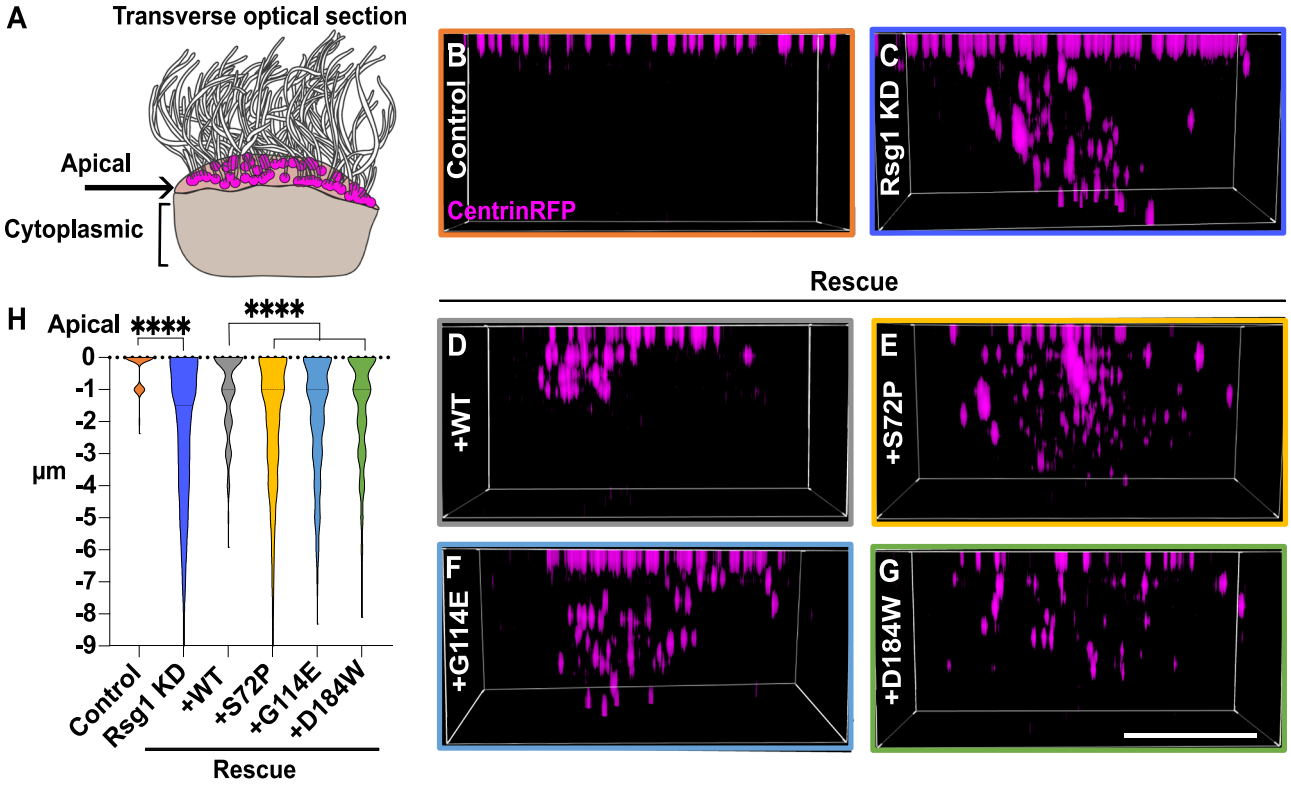

Fig. 4 | Ciliopathy-associated alleles of *RSG1* disrupt basal body docking. **A** Schematic representation of a MCC, depicting the apical and cytoplasmic regions shown in transverse optical section in this figure. **B**–**G** Transverse 3D projection of centrin (magenta), scale bar = 5 µm. **H** Graph shows the distribution of basal body depth below the apical surface in µm. $N > 18$ cells in 6 embryos across 2 experiments for all conditions. *N* values and statistics can be found in Supplementary Dataset 3.

This interaction prompted us to further explore the interplay of Rsg1 and Fam92.

Rsg1 recruits Fam92b specifically to docking basal bodies

There are two Fam92 paralogues (Fam92a and Fam92b) which display distinct patterns of expression, and we first examined Fam92b since it is expressed strongly in *Xenopus* MCCs[57]. We found that knockdown of Rsg1 led to a partial but significant reduction of Fam92b from basal bodies in *these cells* (Fig. 8A–C). To confirm this result, we also expressed $Rsg1^{T65N}$, which we previously showed to disrupt ciliogenesis[16], and this, too, disrupted localization of Fam92b to basal bodies (Fig. 8D–F). This result was specific to Fam92b, as the distal appendage marker Cep164 was not reduced (Supplementary Fig. 7A-C), consistent with previous data that loss of the upstream CPLANE subunit Jbts17 also does not disrupt Cep164[23].

These results prompted us to determine the dynamics of these proteins' localization to migrating and docking basal bodies. We found that while Rsg1 and Ift43 were present on BBs before and after docking in normal *Xenopus* MCCs (Supplementary Fig. 7D, E), Fam92b was present only at very low levels in undocked, migrating basal bodies but accumulated dramatically on docked basal bodies (Fig. 8G–H). Since data from mouse suggest that Rsg1 functions specifically in late steps in ciliogenesis[22], our data suggest that loss of Rsg1 disrupts ciliogenesis at least in part by blocking the late addition of Fam92b to basal bodies.

Human RSG1 controls ciliogenesis and FAM92a recruitment

Rsg1 is essential for ciliogenesis in *Xenopus* and mice[16,22], but neither its role in human cells nor its relationship to Fam92 have yet been tested. We therefore used CRISPR to generate two distinct *CPLANE2/RSG1* knockout lines in human RPE1 cells (Supplementary Fig. 8A, B). In both lines, Rsg1 loss resulted in roughly 75% reduction of ciliation as indicated by immunostaining for Arl13b and AcTub (Fig. 9A–C, G). Moreover, FAM92A recruitment to basal bodies was severely, if not completely, reduced in each of the *RSG1* KO lines (Fig. 9D–F, H). This result was specific, as neither line displayed loss of the centrosomal protein Cep192 (Fig. 9D–F). These data suggest that the disease phenotypes we observed in patients with variants in *RSG1* (Fig. 1) indeed result from loss of cilia and that they are related at least in part to loss of FAM92a from basal bodies.

CPLANE proteins recruit transition zone components

Fam92a is present at mammalian ciliary transition zone (TZ), but its role at this location has been well-defined only in *Drosophila*[46,47,50]. The loss of FAM92A from basal bodies after RSG1 loss therefore prompted us to ask if the CPLANE complex may be more generally involved in TZ architecture in mammalian cells. NPHP1 is a canonical TZ marker and a well-known ciliopathy protein[58], and we found that NPHP1 was severely reduced from basal bodies after RSG1 loss in human RPE1 cells (Fig. 10A–C, G), though like FAM92, it was not entirely eliminated.

Finally, we were curious to know if this effect on the TZ was specific to loss of Rsg1, or if it may be a general feature of the larger CPLANE complex. We therefore examined mouse embryonic fibroblast cell lines that were lacking either Fuz or Intu, two other CPLANE subunits[16,18]. Both lines displayed severe defects in ciliogenesis as expected (Supplementary Fig. 8C–G), and both also displayed significant, but not total, loss of Nphp1 from basal bodies (Fig. 10D–F, H). Thus, disruption of normal TZ protein recruitment to basal bodies is a common feature of CPLANE loss and may be related to CPLANE-associated ciliopathy.

Discussion

Here, we have shown that variants in the *CPLANE2/RSG1* gene cause human ciliopathy, and these variants severely disrupt either the localization or the function of Rsg1. We further show that disruption of GTP binding inhibits Rsg1 interaction with other CPLANE

https://doi.org/10.1038/s41467-025-61005-8

		Rsg1	Rsg1^{T69N}	Log2FC
Cplane	Fuz	1024	0	-11.19
	Intu	430	0	-9.21
	Wdpcp	1696	8	-8.51
	Jbts17	898	0	-8.03
Vesicle trafficking	Hps1	208	0	-8.55
	Rab3b	32	0	-7.08
	Rab5c	22	0	-6.49
	Rab29	10	0	-5.7
Actin regulator	Pfn1	12	0	-6.31
	Pdlim4	18	0	-5.86
	Coro1c	20	0	-5.24
Transition Zone	Fam92a	38	0	-7.03
	Dzip1	10	0	-5.98
	Cby1	20	0	-4.44
Non-specific	Ruvbl1	128	100	-0.13
	Eef1a1	448	472	0.3
	Tubb6	1890	2756	0.77
	Hsp90ab1	268	226	-0.02

Fig. 5 | APMS comparison of WT and T69N Rsg1. Spectral counts are shown for selected proteins in APMS with WT Rsg1 versus the Rsg1(T69N) mutant. Interactors are grouped by function. Examples of non-specific interactors are provided at the bottom. Full data table can be found in Supplementary Dataset 3.

components as well as with novel interactors. AlphaFold predicts that one of those, Fam92a, is a novel effector that is recruited to basal bodies by the Rsg1 GTPase. Finally, these results led us to discover that recruitment of transition zone proteins to basal bodies is a shared feature of multiple CPLANE subunits. These data are significant for several reasons.

First, these data shed light on the still enigmatic mechanism of Rsg1 function. Though similar to Rabs, Rsg1 displays many notable differences such as very low catalysis of GTP due to lack of the crucial glutamine in the G3 region[15]. That said, our data strongly suggest that GTP loading is essential, both for CPLANE interaction and for binding to Fam92a (Fig. 5). Moreover, Rabs can simultaneously bind multiple effectors[55], and our data suggest the same is true for Rsg1. Indeed, our APMS and modeling suggest that Fam92a is an Rsg1 effector protein that can bind simultaneously with the known effector Fuz (Fig. 6A–D).

Second, CPLANE is known to affect both retrograde IFT and basal body docking in *Xenopus* [10–12], but only the former had previously been implicated in disease etiology[23]. It is significant, that disease alleles of two CPLANE subunits fail to support basal body docking (Fig. 4; Supplementary Fig. 5). Moreover, the interaction of Rsg1 with Fam92, Cby1 and Dzip1, is notable because like CPLANE proteins, these are also implicated in basal docking and have also been associated with defects in retrograde IFT[49–51]. Further exploration of these proteins' functional interaction will be of interest.

Third, the identification of Fam92 as a CPLANE interactor provides new insight into the complex interplay of proteins and membrane at the base of cilia[59]. Interestingly, the CPLANE subunits Fuz, Intu, and Wdpcp, but not Rsg1 can directly interact with lipids, especially PI(3)P, PI(4)P, and PI(5)P[15]. Rsg1 does not bind directly to lipids, so it is interesting that it does bind directly to Fam92, whose BAR domains bind and tubulate negatively charged lipids in vitro[53]. Moreover, Fam92 interacts with lipids via a series of lysine and arginines on the concave face of the dimer[53], while Rsg1 and Fuz are positioned opposite, on the convex side (Supplementary Fig. 6D). Thus, Rsg1 could interact with lipid-engaged

Fam92, providing a possible route to recruitment of CPLANE to curved membrane surfaces. These findings complement previous work on BAR-domain proteins in ciliogenesis, such as MiniBAR and Pacsins[60,61].

Finally, these data provide insights into the molecular basis of the wide range of multi-organ congenital disorders termed ciliopathies[62], including OFD, a genetically heterogeneous ciliopathy characterized by anomalies of the oral cavity, face, and digits. Affected individuals may also present additional malformations including cerebral and/or cerebellar structural anomalies, cystic renal disease, and skeletal and ocular anomalies[63]. Our work describes three individuals with OFD phenotype from three unrelated families in whom four distinct variants in CPLANE2 were identified. These OFD-affected individuals showed no other variants in genes previously associated with this condition after exome sequencing. Individuals one and two of our series presented with cardinal orofacial and digital OFD features in addition to variable expressivity of other clinical phenotypes. In contrast, individual 3 presented with a milder phenotype including OFD manifestations but not all of the cardinal ones. Importantly, our functional studies are consistent with this observation, as the milder phenotype observed in participant 3 correlates with less severe disruption in IFT recruitment and basal body docking in comparison with individuals one and two. Thus, our work suggests RSG1 is an OFD locus, and this locus should be investigated in additional cases of OFD syndrome to allow a better delineation of the phenotype, follow-up, and the appropriate genetic counselling to the families.

Methods

All research was performed in compliance with relevant ethical regulatory bodies at each institution.

Patients

We detected three patients with a phenotype consistent with ciliopathy and with homozygous or compound heterozygous variants in *RSG1* from three different centers. Clinical investigators were contacted through GeneMatcher, which enables new gene phenotype connections[64]. All clinical and molecular data were collected including prenatal, morphologic, and neurodevelopmental characteristics as well as previous genetic studies. Informed consent approved by the local IRB was signed by their legal guardians.

Patient genetic analysis

Exome sequencing (ES) was performed for all patients according to the protocols and platforms of each center. Evaluation of ES variants excluded pathogenic changes in previously described OFD genes in any of the probands, which prompted us to search for a new gene responsible for this condition. In general, the identification of CPLANE2 variants in the sequencing data was done by filtering for: 1) variants with an ultra-rare allele frequency in the population (not present in gnomAD) and/or 2) variants located in exonic regions or splice sites. Interpretation of single nucleotide variants was done according to ACMG guidelines 4[65].

Xenopus embryo manipulations

Follow-up experiments on select candidates were performed in *Xenopus laevis*. All *Xenopus* experiments were conducted in accordance with the animal protocol AUP-2024-00130 and the animal ethics guidelines of the University of Texas at Austin.

Female adult *Xenopus laevis* were injected with human chorionic gonadotropin the night preceding experiments to induce ovulation. Females were squeezed to lay eggs, and eggs were fertilized in vitro with homogenized testis in 1/3X Marc's modified Ringer's (MMR). Two-cell stage embryos were de-jellied in 1/3X MMR with 2.5% (wt/vol) cysteine (pH 7.9), then washed and maintained in 1/3X MMR solution. For plasmid, mRNA microinjections, embryos were placed in 2% Ficoll in 1/3X MMR and injected using a glass needle, forceps, and an Oxford universal micromanipulator. After injection, embryos

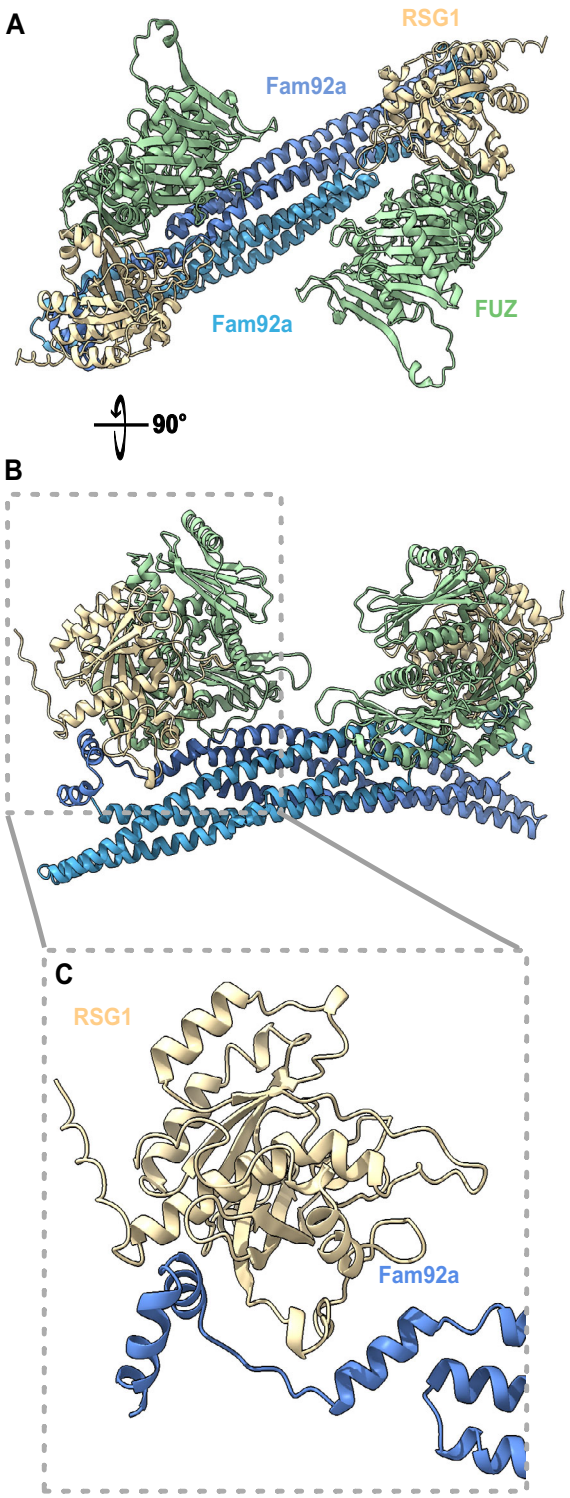

Fig. 6 | AlphaFold3 predicts direct interaction of RSG1 with FAM92A. **A** Alphafold3 prediction of the structure of two human FUZ-RSG1 heterodimers interacting with one Fam92a homodimer. Colors indicate monomers as indicated. **B** 90-degree rotation from (**B**). **C** Increased magnification view of (**C**) showing the RGS1-FAM92A interaction (after removal of FUZ and one copy of FAM92A for clarity).

https://doi.org/10.1038/s41467-025-61005-8

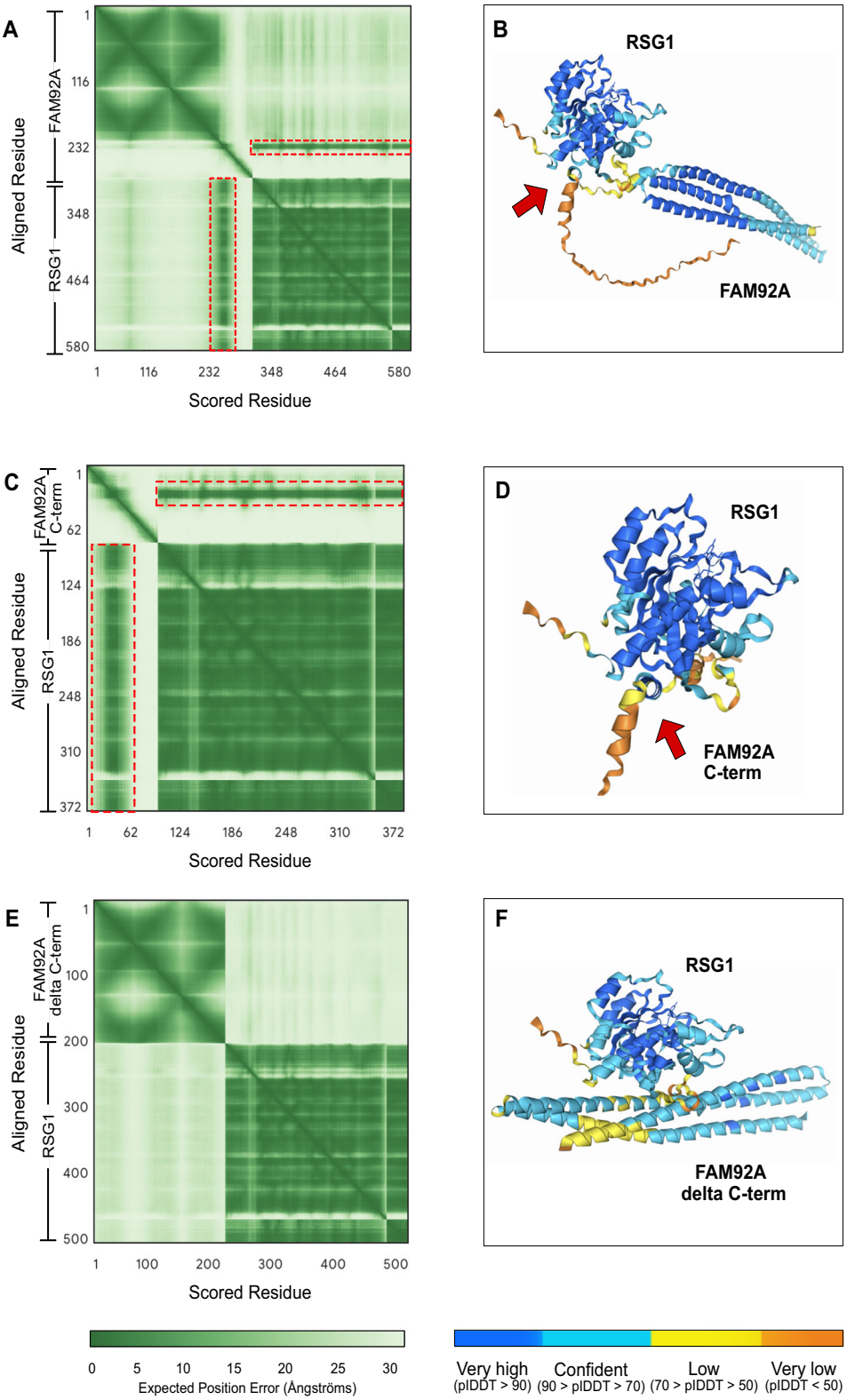

Fig. 7 | Quantification of AlphaFold3 structure predictions. A PAE Plot for the interaction of full-length human RSG1 and FAM92A monomers; arrow indicates region of Rsg1 interaction with the C-terminus of Fam92. **B** Structure of RSG1 monomer in complex with FAM92A monomer, with colors indicating PlDDT. **C** PAE Plot for the interaction of full-length RSG1 with the C-terminal 83 amino acids of FAM92A; arrow indicates region of Rsg1 interaction. **D** Structure corresponding to C, with colors indicating PlDDT. **E** PAE Plot indicates no interaction between full-length RSG1 with the C-terminal 83 amino acids of FAM92A; arrow indicates region of Rsg1 interaction. **F** Structure corresponding to E, note very poor PlDDT scores at the region of "interface.".

https://doi.org/10.1038/s41467-025-61005-8

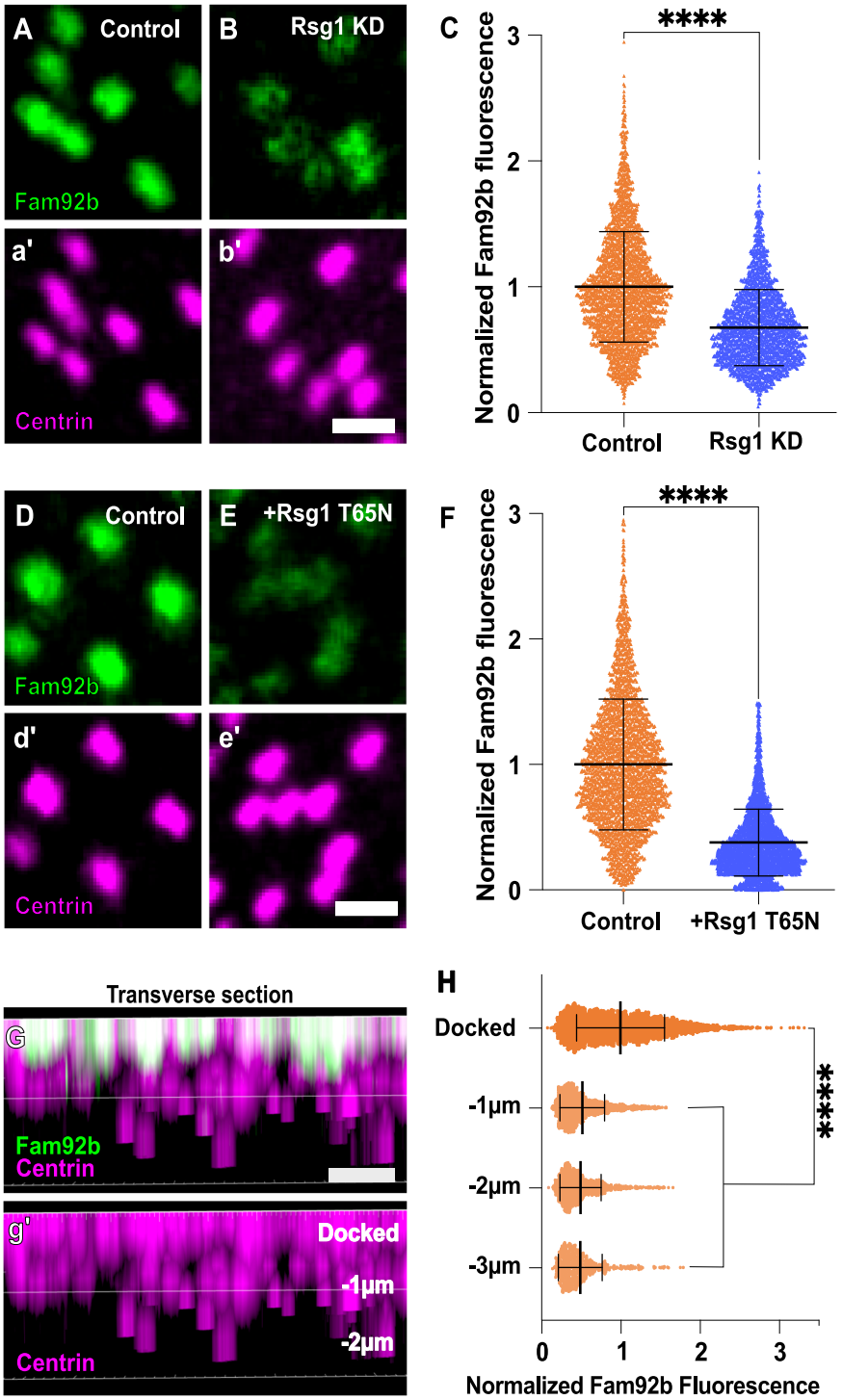

Fig. 8 | Rsg1 recruits Fam92b to docking basal bodies in *Xenopus* MCCs. **A**, **B**, **D**, **E** High magnification *en face* images of MCCs apical basal bodies labeled by centrin (magenta) and Fam92b (green) scale bar = 1 µm. **C**, **F** Graphs of normalized Fam92b basal body fluorescence. **C** Graph showing Fam92b fluorescence levels after KD of Rsg1. **F** Graph showing Fam92b fluorescence levels after over expression of Rsg1 T65N. **G** Transverse 3D projection of centrin (magenta) and Fam92b (green), scale bar = 5 µm. **H** Graph shows the fluorescence intensity of Fam92b on basal bodies at different depths starting from apical (docked) and several µm from the apical surface. $N > 25$ cells in 6 embryos across 3 experiments for all conditions. All graphs show showing mean ± standard deviation. N values and statistics can be found in Supplementary Dataset 3.

were kept in Ficoll for at least 30 min and removed from Ficoll solution to develop in 1/3 MMR solution.

Plasmid, mRNA, and MO microinjections

Plasmids containing GFP-Ift43, GFP-Rsg1, Flag-Rsg1 WT, T65N, and for all patient alleles (S72P, D184W, G114E), GFP and mScarlet3-Fam92b, GFP-Cep164, and Centrin-RFP or BFP were used for mRNA synthesis[12]. To generate a *Xenopus* allele corresponding to the human patient allele, mutagenesis was performed on the GFP and FLAG-tagged Xenopus Rsg1, using Q5 Site-Directed Mutagenesis Kit (NEB, Cat # E0554S). Capped mRNAs were synthesized using the mMESSAGE mMACHINE SP6 transcription kit (Thermo Fisher Scientific, Cat #

https://doi.org/10.1038/s41467-025-61005-8

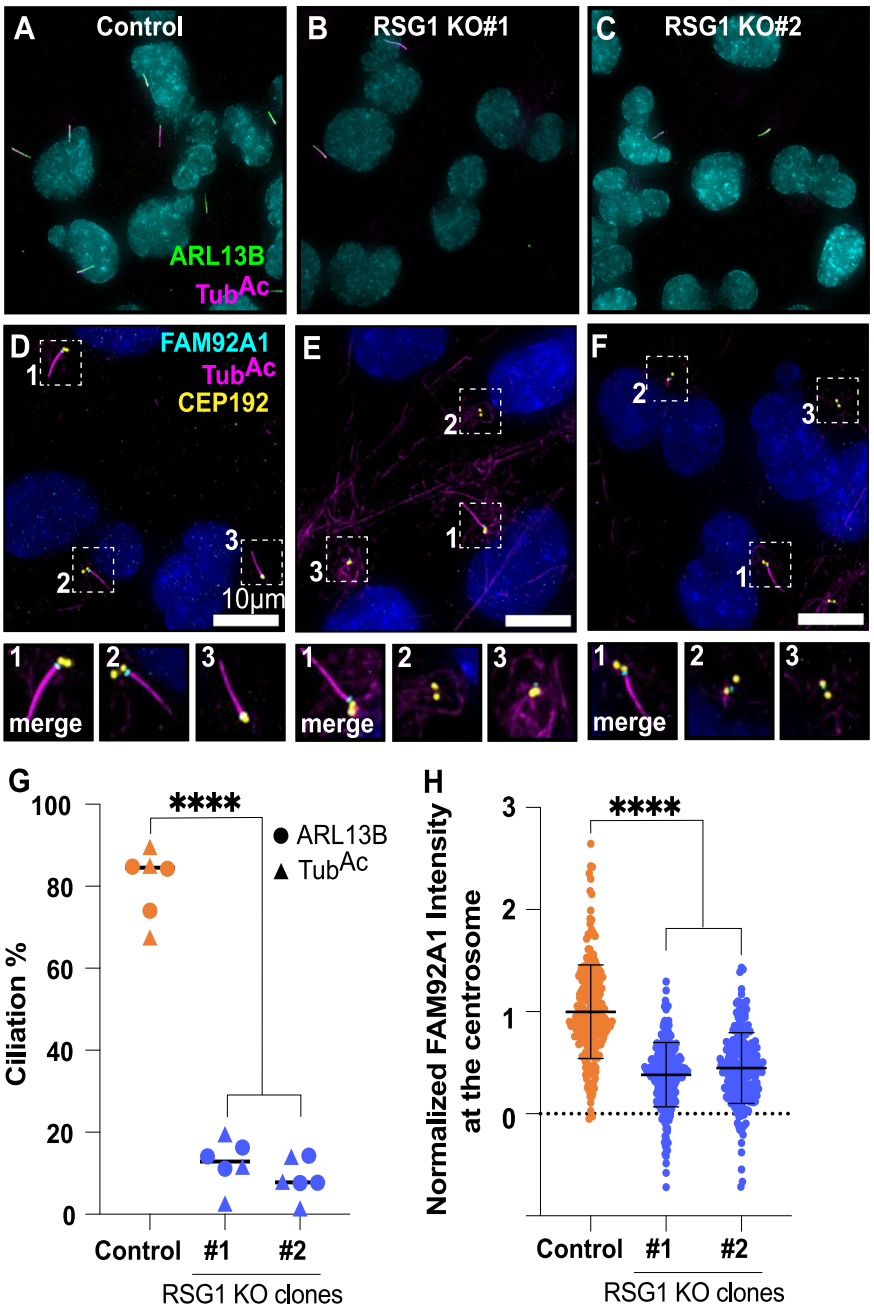

Fig. 9 | RSG1 is required for ciliogenesis and recruitment of FAM92A to basal bodies in human cells. A–C Human RPE1 cells stained for ARL13B (green) and TubAc (magenta) as markers in control and RSG1 crispant cells. scale bar = 10 μm **D–F** Imaging of FAM92A (cyan) fluorescence at the transition zone CEP192 (yellow) in RPE1 cells with mutated Rsg1. Insets show three indicated cilia from the panels above. **G** Percentage ciliation using ARL13B (green) and TubAc (magenta) positive cells in RSG1 mutants. **H** Mean ± standard deviation of normalized FAM92 at the transition zone, ciliated cells marked in orange and non-ciliated in blue. $N > 80$ for all conditions. N values and statistics can be found in Supplementary Dataset 3.

AM1340). Translation-blocking Rsg1 morpholino (5′-GGCCCGTATCT CTGTAGTGCAGCAA–3′) (Gene Tools) has been previously described[12,16]. mRNA and/or morpholino were injected into two ventral blastomeres at the four-cell stage to target the epidermis. mRNAs were injected at 40–100 pg per blastomere, and morpholino was injected at 30 ng per blastomere.

In vitro pull-down assay

GFP-Rsg1, Myc-Fam92a, and GFP were in vitro translated using plasmid containing their respective open reading frames (ORFs) with the T_NT SP6 Hig-Yield Wheat Germ Protein Expression System (Promega Cat# L3261). The in vitro translated GFP-tagged and Myc-tagged proteins were first incubated together in binding/wash buffer (25 mM Tris pH 7.5, 150 mM NaCl, 2 mM $MgCl_2$, 0.05% Triton X-100), followed by immunoprecipitation using ChromoTek GFP-Trap agarose beads (Proteintech, Cat# GTA20). The immunoprecipitated samples were then analyzed by SDS-PAGE. The input and immunoprecipitated(IP) samples were analyzed by SDS-PAGE and immunoblotted with the following antibodies: anti-GFP antibody (Santa Cruz, Cat# sc-9996), HRP-conjugated goat anti mouse IgG (H + L) secondary antibody (ThermoFiser Scientific, Cat# 31430), anti-MYC antibody (Abcam, cat#ab9106), and HRP-conjugated affinipure Goat Anti-Rabbit IgG(H + L) (Proteintech, Cat#SA00001-2).

https://doi.org/10.1038/s41467-025-61005-8

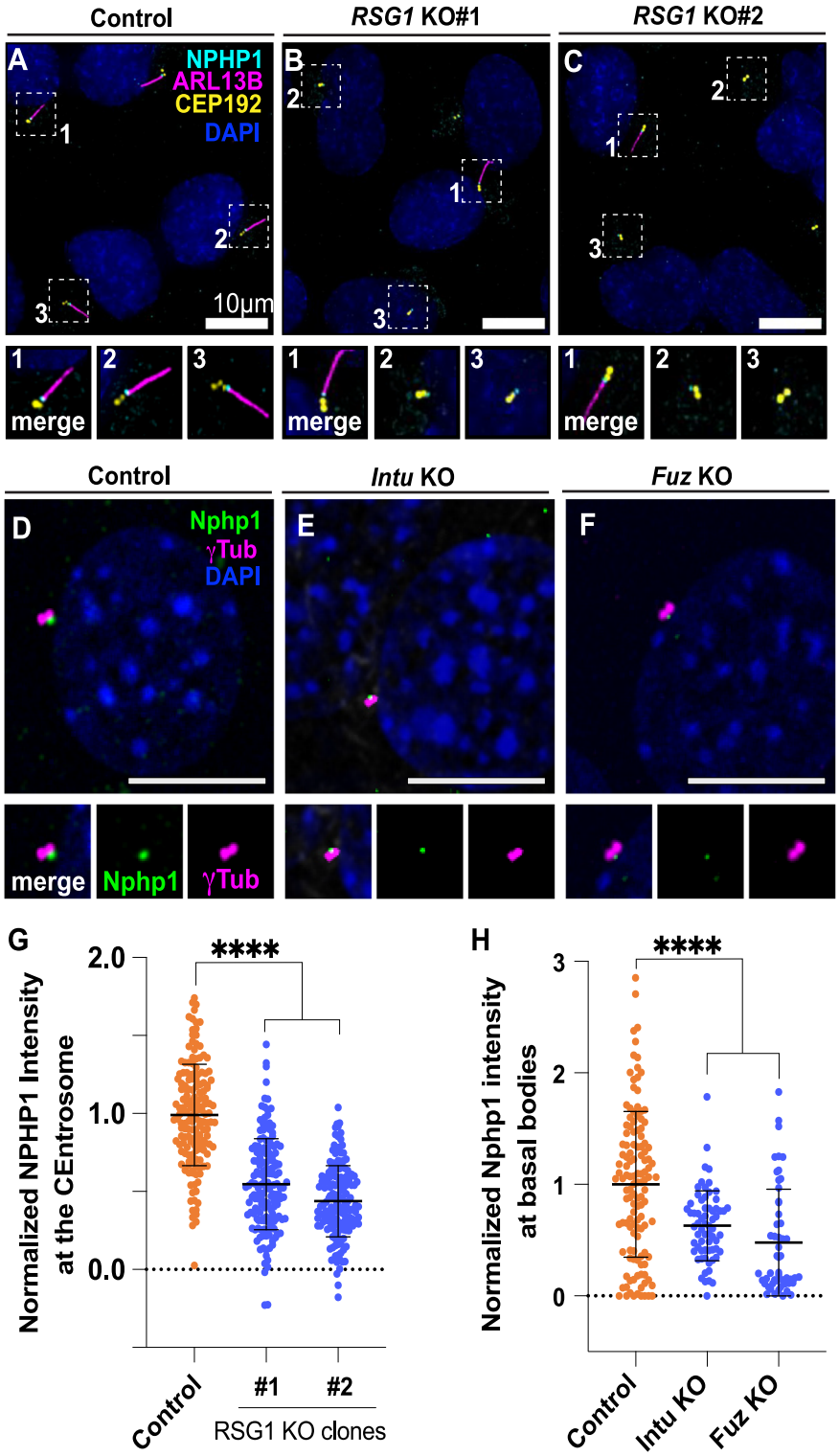

Fig. 10 | CPLANE is required for normal recruitment of the transition zone to the basal body. A–**C** Human RPE1 cells stained for the TZ protein NPHP1, the basal body protein Cep192, and the cilia marker ARL13B. Scale bar = 10 µm. **G** Graph shows mean ± standard deviation of normalized Nphp1 fluorescence at the transition zone for indicated genotypes. **D**–**F** Nphp1(green) fluorescence at basal bodies labeled in tub(magenta) in *Intu or Fuz* mutant mouse embryo fibroblasts. Scale bar = 10 µm. **H** Graph shows mean ± standard deviation of normalized Nphp1 fluorescence at the basal body in controls and *Intu* or Fuz mutants. *N* > 52 for all conditions. *N* values and statistics can be found in Supplementary Dataset 3.

Immunoblotting

Embryos were lysed in Lysis buffer (ThermoFisher Scientific, Cat# 78501) containing protease inhibitors. The lysates were centrifuged to remove cell debris, and the supernatants were subjected to SDS-PAGE followed by immunoblotting using standard protocols. The antibodies used were as follows: anti-GFP antibody (Santa Cruz, Cat# sc-9996), HRP-conjugated goat anti mouse IgG (H + L) secondary antibody (ThermoFiser Scientific, Cat# 31430), beta actin monoclonal antibody (Proteintech, Cat # 6009-1).

Live imaging and image analysis for *Xenopus*

For live imaging, *Xenopus* embryos (stage 25) were mounted between two coverslips and submerged in 0.01% benzocaine in 1/3X MMR and imaged on a Zeiss LSM700 confocal microscope using a Plan-Apochromat 63 × 1.4 NA oil DIC M27 immersion lens. Data for Rsg1 allele localization, spatiotemporal of (Ift43, Rsg1, Fam92b), and Fam92b under Rsg1 KD and Rsg1 T65N overexpression experiments all include three replicates. Data for Rsg1 rescue of IFT43 and docking phenotype, and Cep164 under Rsg1 KD data represent two replicates. A more detailed number of embryos, cells, and basal bodies quantified can be found for each experiment in Supplementary Dataset 3.

Images were processed using the Fiji distribution of ImageJ, and figures were assembled in Affinity Designer.

Quantification of fluorescence intensity of basal body localizing proteins was performed on micrographs taken at the single z-depth which best captured the most basal bodies as labeled by centrin- RFP. Quantification performed on single z micrographs for both basal body localization of both Rsg1 alleles and IFT43 rescue data.

Fluorescence intensity was measured by first duplicating the centrin-RFP channel and using the duplicate to reduce background signal as well as smoothing the image to then analyze particles. Measurements were then taken by using the particle analysis ROIs on the GFP-tagged candidate protein and centrin-RFP raw channels independently using the "Measure" function. Normalization was performed by calculating the ratio of candidate GFP intensity to the centrin-RFP intensity and normalizing all data sets to the control average.

Tandem affinity purification

5 mL packed cell volume of IMCD3 cells expressing LAPN-tagged proteins were re-suspended with 20 mL of LAP-resuspension buffer (300 mM KCl, 50 mM HEPES-KOH [pH 7.4], 1 mM EGTA, 1 mM MgCl2, 10% glycerol, 0.5 mM DTT, protease inhibitor [A32965, Thermo Fisher Scientific]), lysed by gradually adding 600 mL 10% NP-40 to a final concentration of 0.3%, then incubated on ice for 10 min. The lysate was first centrifuged at 14,000 rpm (27,000 g) at 4 °C for 10 min, and the resulting supernatant was centrifuged at 43,000 rpm (100,000 g) for 1 hr at 4 °C to further clarify the lysate. High speed supernatant was mixed with 500 µl of GFP-coupled beads[66] and rotated for 1 hr at 4 °C to capture GFP-tagged proteins, then washed five times with 1 mL LAP200N buffer (200 mM KCl, 50 mM HEPES-KOH [pH 7.4], 1 mM EGTA, 1 mM MgCl2, 10% glycerol, 0.5 mM DTT, protease inhibitors, and 0.05% NP40). After re-suspending the beads with 1 mL LAP200N buffer lacking DTT and protease inhibitors, the GFP tag was cleaved by adding 40 µg TEV protease and rotating tubes at 4 °C for 16 h. TEV-eluted supernatant was added to 100 µL of S-protein agarose (69704-3, EMD Millipore) to capture S-tagged protein. After washing three times with LAP200N buffer lacking DTT and twice with LAP0 buffer (50 mM HEPES-KOH [pH 7.4], 1 mM EGTA, 1 mM MgCl2, and 10% glycerol), purified protein complexes were eluted with 50 µL of 2X LDS buffer and boiled at 95 °C for 3 min. Samples were then run on Bolt Bis-Tris Plus Gels (NW04120BOX, Thermo Fisher Scientific) in Bolt MES SDS Running Buffer (B0002, Thermo Fisher Scientific). Gels were fixed in 100 mL of fixing solution (50% methanol, 10% acetic acid in Optima LC/MS grade water [W6-4, Fisher Scientific]) at room temperature, and stained with Colloidal Blue Staining Kit (LC6025, Thermo Fisher Scientific). After the buffer was replaced with Optima water, the bands were cut into eight pieces. The gel slices were then destained, reduced, and alkylated followed by in-gel digestion using (125 ng) Trypsin/LysC (V5073, Promega) as previously described[67]. Tryptic peptides were extracted from the gel bands and dried in a speed vac. Prior to LC-MS, each sample was reconstituted in 0.1% formic acid, 2% acetonitrile, and water.

Mass spectrometry

Samples were run on Thermo Orbitrap Fusion at Stanford University Mass Spectrometry (SUMS).

Data analysis

Raw mass spec result files were processed using Bionic (Protein Metrics, Inc.) software (version: v2.16.11) with the following parameters: precursor mass tolerance: 20 ppm, fragment mass tolerance: 40 ppm; fragmentation type: QTOF/HCD; propionamide as Cys fixed modification, variable modifications of Met, His and Trp oxidation, Asn and Gln deamidation, and Ser, Thr and Tyr phosphorylation, with maximum 2 variable modification; trypsin with maximum 2 missed cleavages and fully specific mode; identifications were filtered at 0.01 FDR at the protein level; a FASTA library of all human refseq proteins (curated and predicted) was used that was downloaded on 2018/06/18.

Spectral counts were converted to normalized spectral abundance factor (NSAF) values[68] and significance of enrichment of bait-association was calculated, and protein interaction networks were constructed in Cytoscape, as previously described[69].

Protein structure modeling

Modeling was performed using AlphaFold3[34] and AlphaFold2[54], and computational alanine scanning was performed using BAlas[70].

Human and mouse cell culture

RPE1 *RSG1* knockout cell lines were generated using two single guide RNAs synthesized by Synthego (sgRNA cut site 1: UUGCCCUAGGGCUGCUUGAG, sgRNA cut site 2: CCCACUCACCGGUGGUCUCG). Thermo Fisher Scientific Neon Transfection System was used for electroporation of sgRNAs with Truecut Cas9 v2. Monoclonal cell line DNA was isolated with QuickExtract DNA Extraction Solution, the cut site was amplified with PCR primers around the deletion site (Forward primer TTGTGTTAGGCCCCACTTCC, reverse primer GACCAAGGAGCCCATGTAGG) and Sanger sequenced to identify insertions or deletions at the cut sites. Monoclonal *RSG1* knockout cell lines were further validated with RT-qPCR to quantify fold change of *RSG1* expression (Forward primer ATCATATGCTGCTGGCTTGC, reverse primer TGGTCAAATTTGGAGCCGATG; forward primer spans exon-exon junction). RNA was isolated with Qiagen RNeasy Mini Kit, and cDNA was synthesized with BioRad iScript cDNA Synthesis Kit. PowerUp SYBR Green Master Mix was used to amplify the target and control cDNA sequences.

MEFs were grown in Advanced DMEM supplemented with 10% FBS, 1% GlutaMax, and 1% antibiotic-anti-mycotic.

Immunostaining

RPE1 cells were grown on glass coverslips (Azer Scientific Inc., ES0117520) and fixed with either 4% PFA (Thomas Scientific, C993M24 or a combination of 1.5% PFA (diluted in 1x PBS) at RT for 4 min, followed by ice-cold MeOH at −20 °C for 4 min. Cells were blocked in blocking solution (2.5% FBS, 200 mM glycine, 0.1% Triton X-100 in PBS) for 1 h at RT. Cells were then incubated in primary antibody diluted in the blocking solution for 1 h and rinsed with PBST (0.1% Triton X-100 in PBS), followed by secondary antibody staining prepared in blocking solution for 1 h and rinsed with PBST. DNA was stained with Hoechst 33342 (Thermo Fisher, H21492), and cells were mounted in ProLong Diamond Antifade Mountant (Fisher Scientific, P36970). Immunofluorescence images were acquired at room temperature (25 °C) using a DeltaVision Elite (GE Healthcare) controlling a pco.edge sCMOS camera with near-perfect linearity across its 15-bit dynamic range. Images were acquired with a Plan Apochromat 60× 1.40 NA oil objective lens with 0.2-µm z-sections. All image acquisition was done in SoftWoRx (6.0; GE Healthcare).

Mouse embryonic fibroblasts (MEFs) were isolated from E12.5embryos. Manually dissociated cells were plated in 6-well tissue culture dishes in DMEM supplemented with 10% fetal bovine serum. After two passages, 2.5 × 10^5 cells were plated onto a coverslip and grown for 24 h to allow cells to re-adhere. MEFs were plated on glass coverslips, grown to confluence, and starved for 24 h in OptiMEM. Cells were fixed for 10 min at RT with 4% PFA in PBS, followed by methanol for 3 min at −20 °C. After fixation, cells were blocked for 1 h at RT or overnight at 4 °C in dPBS + 0.1% Triton X-100 + 2.5% BSA (IF block). Cells were incubated with primary antibodies diluted in IF block overnight at 4 °C. Coverslips were washed with dPBS and then incubated with Alexa-conjugated secondary antibodies raised in goat or donkey (Invitrogen) at RT. After three dPBS washes, coverslips were mounted using ProLong Gold antifade (Invitrogen) and sealed with nail polish. Cells were imaged with a TCS SP5 microscope (Leica) or Zeiss LSM700 confocal.

Antibodies

The following antibodies were used for RPE1 cells: rabbit-NPHP1 (1:200, Sigma-Aldrich, SAB1401267), rabbit-FAM92A1 (1:200, Thermo Fisher Scientific, 24803-1-AP), mouse-acetylated Tubulin (1:1000, Santa Cruz Biotechnology, sc-23950), goat-CEP192 (1:2000; gift from Andrew Holland's lab, raised against CEP192 [amino acids 1–211]). Secondary antibodies conjugated to Alexa Fluor 488, 568, or 647 were used (1:1000, Life Technologies Corporation).

The following antibodies were used for MEFs: rabbit α-Nphp1 (gift of G. Pazour, University of Massachusetts Medical School, Worcester, MA; amino acids 1–209 [Benzing et al., 2001; Fliegauf et al., 2006]), rabbit α-Arl13b (Proteintech, cat# 17711-1-AP), goat α−γ-tubulin (Santa Cruz Biotechnology, Inc., cat# sc-7396), mouse α-detyrosinated tubulin (Millipore, cat# ab254154).

Image analysis of NPHP1 and ciliogenesis

For quantitation of signal intensity at the centrosome in RPE1 cells, deconvolved 2D maximum intensity projections were saved as 16-bit TIFF images. Signal intensity was determined by drawing a circular region of interest (ROI) around the centriole (small ROI [ROI_S]). A larger concentric circle (large ROI [ROIL]) was drawn around ROI_S. ROI_S and ROI_L were transferred to the channel of interest, and the signal in ROI_S was calculated using the formula $I_S - [(I_L - I_S)/(A_L - A_S) \times A_S]$, where A is area and I is integrated intensity.

FIJI (FIJI is Just ImageJ) was used for image analysis of MEFs. To quantify ciliogenesis, the total number of cilia and nuclei were manually counted, and % ciliation was calculated. For transition zone localization of NPHP1, a circle was used to measure the integrated density of NPHP1 and gTub for every basal body in the image. The background intensity was also calculated for each channel. For both NPHP1 and gTub, the background intensity was subtracted from the experimental intensity. Then, the corrected NPHP1 intensity was normalized to the corrected gTub intensity.

Reporting summary

Further information on research design is available in the Nature Portfolio Reporting Summary linked to this article.

Data availability

All proteomic data are available in the PRIDE database (Project accession: PXD055830; Project DOI: 10.6019/PXD055830).All image analysis data are available in the supplementary Source Data file. Source data are provided with this paper.

References

1. Hildebrandt, F., Benzing, T. & Katsanis, N. Ciliopathies. *N. Engl. J. Med.* **364**, 1533–1543 (2011).
2. Reiter, J. F. & Leroux, M. R. Genes and molecular pathways underpinning ciliopathies. *Nat. Rev. Mol. Cell Biol.* **18**, 533–547 (2017).
3. Mitchison, H. M. & Valente, E. M. Motile and non-motile cilia in human pathology: from function to phenotypes. *J. Pathol.* **241**, 294–309 (2017).
4. Ishikawa, H. & Marshall, W. F. Intraflagellar transport and ciliary dynamics. *Cold Spring Harb. Perspect. Biol.* **9** https://doi.org/10.1101/cshperspect.a021998 (2017).
5. Klena, N. & Pigino, G. Structural biology of cilia and intraflagellar transport. *Annu Rev. Cell Dev. Biol.* **38**, 103–123 (2022).
6. Tian, X., Zhao, H. & Zhou, J. Organization, functions, and mechanisms of the BBSome in development, ciliopathies, and beyond. *Elife* **12** https://doi.org/10.7554/eLife.87623 (2023).
7. Reiter, J. F., Blacque, O. E. & Leroux, M. R. The base of the cilium: roles for transition fibres and the transition zone in ciliary formation, maintenance and compartmentalization. *EMBO Rep.* **13**, 608–618 (2012).
8. Adler, P. N. & Wallingford, J. B. From planar cell polarity to ciliogenesis and back: the curious tale of the PPE and CPLANE proteins. *Trends Cell Biol.* **27**, 379–390 (2017).
9. Park, T. J., Haigo, S. L. & Wallingford, J. B. Ciliogenesis defects in embryos lacking inturned or fuzzy function are associated with failure of planar cell polarity and Hedgehog siere mrmrgnaling. *Nat. Genet.* **38**, 303–311 (2006).
10. Park, T. J., Mitchell, B. J., Abitua, P. B., Kintner, C. & Wallingford, J. B. Dishevelled controls apical docking and planar polarization of basal bodies in ciliated epithelial cells. *Nat. Genet.* **40**, 871–879 (2008).
11. Brooks, E. R. & Wallingford, J. B. Control of vertebrate intraflagellar transport by the planar cell polarity effector Fuz. *J. Cell Biol.* **198**, 37–45 (2012).
12. Brooks, E. R. & Wallingford, J. B. The small GTPase Rsg1 is important for the cytoplasmic localization and axonemal dynamics of intraflagellar transport proteins. *Cilia* **2**, 13 (2013).
13. Gerondopoulos, A. et al. Planar cell polarity effector proteins inturned and fuzzy form a Rab23 GEF complex. *Curr. Biol.* **29**, 3323–3330.e3328 (2019).
14. Sanchez-Pulido, L. & Ponting, C. P. Hexa-Longin domain scaffolds for inter-Rab signalling. *Bioinformatics* **36**, 990–993 (2020).
15. Langousis, G. et al. Structure of the ciliogenesis-associated CPLANE complex. *Sci. Adv.* **8**, eabn0832 (2022).
16. Gray, R. S. et al. The planar cell polarity effector Fuz is essential for targeted membrane trafficking, ciliogenesis and mouse embryonic development. *Nat. Cell Biol.* **11**, 1225–1232 (2009).
17. Kim, S. K. et al. Planar cell polarity acts through septins to control collective cell movement and ciliogenesis. *Science* **329**, 1337–1340 (2010).
18. Zeng, H., Hoover, A. N. & Liu, A. PCP effector gene Inturned is an important regulator of cilia formation and embryonic development in mammals. *Dev. Biol.* **339**, 418–428 (2010).
19. Heydeck, W. & Liu, A. PCP effector proteins inturned and fuzzy play nonredundant roles in the patterning but not convergent extension of mammalian neural tube. *Dev. Dyn.* **240**, 1938–1948 (2011).
20. Cui, C., Chatterjee, B., Lozito, T., Zhang, Z. & Lo, C. W. Wdpcp, a PCP protein required for ciliogenesis, regulates directional cell migration and cell polarity by direct modulation of the actin cytoskeleton. *PLoS Biol.* **11**, e1001720 (2013).
21. Engelhardt, D., Marean, A., McKean, D., Petersen, J. & Niswander, L. RSG1 is required for cilia-dependent neural tube closure. *Genesis* **62**, e23602 (2024).
22. Agbu, S. O., Liang, Y., Liu, A. & Anderson, K. V. The small GTPase RSG1 controls a final step in primary cilia initiation. *J. Cell Biol.* **217**, 413–427 (2018).
23. Toriyama, M. et al. The ciliopathy-associated CPLANE proteins direct basal body recruitment of intraflagellar transport machinery. *Nat. Genet.* **48**, 648–656 (2016).

24. Martín-Salazar, J. E. & Valverde, D. CPLANE complex and ciliopathies. *Biomolecules* **12** https://doi.org/10.3390/biom12060847 (2022).
25. Bruel, A. L. et al. INTU-related oral-facial-digital syndrome type VI: a confirmatory report. *Clin. Genet* **93**, 1205–1209 (2018).
26. Yakar, O. & Tatar, A. INTU-related oral-facial-digital syndrome XVII: clinical spectrum of a rare disorder. *Am. J. Med. Genet. A* **188**, 590–594 (2022).
27. Zhang, W. et al. Expanding the genetic architecture and phenotypic spectrum in the skeletal ciliopathies. *Hum. Mutat.* **39**, 152–166 (2018).
28. Lopez, E. et al. C5orf42 is the major gene responsible for OFD syndrome type VI. *Hum. Genet.* **133**, 367–377 (2014).
29. Shaheen, R. et al. Genomic analysis of Meckel-Gruber syndrome in Arabs reveals marked genetic heterogeneity and novel candidate genes. *Eur. J. Hum. Genet.* **21**, 762–768 (2013).
30. Saari, J., Lovell, M. A., Yu, H. C. & Bellus, G. A. Compound heterozygosity for a frame shift mutation and a likely pathogenic sequence variant in the planar cell polarity—ciliogenesis gene WDPCP in a girl with polysyndactyly, coarctation of the aorta, and tongue hamartomas. *Am. J. Med. Genet. A* **167a**, 421–427 (2015).
31. Steichen-Gersdorf, E., Gassner, I., Covi, B. & Fischer, H. Oral-facial-digital syndrome II. Transitional type between Mohr and Majewski syndrome: report of a new case with congenital stenosis of the trachea. *Clin. Dysmorphol.* **3**, 245–250 (1994).
32. Zheng, D. et al. Predicting the translation efficiency of messenger RNA in mammalian cells. *bioRxiv*, 2024.2008.2011.607362 https://doi.org/10.1101/2024.08.11.607362 (2024).
33. Tabler, J. M. et al. Cilia-mediated Hedgehog signaling controls form and function in the mammalian larynx. *Elife* **6** https://doi.org/10.7554/eLife.19153 (2017).
34. Abramson, J. et al. Accurate structure prediction of biomolecular interactions with AlphaFold 3. *Nature* **630**, 493–500 (2024).
35. Cheng, J. et al. Accurate proteome-wide missense variant effect prediction with AlphaMissense. *Science* **381**, eadg7492 (2023).
36. Walentek, P. & Quigley, I. K. What we can learn from a tadpole about ciliopathies and airway diseases: Using systems biology in Xenopus to study cilia and mucociliary epithelia. *Genesis* **55** https://doi.org/10.1002/dvg.23001 (2017).
37. Rao, V. G. & Kulkarni, S. S. Xenopus to the rescue: a model to validate and characterize candidate ciliopathy genes. *Genesis* **59**, e23414 (2021).
38. Srour, M. et al. Mutations in C5ORF42 cause Joubert syndrome in the French Canadian population. *Am. J. Hum. Genet.* **90**, 693–700 (2012).
39. Gerondopoulos, A., Langemeyer, L., Liang, J. R., Linford, A. & Barr, F. A. BLOC-3 mutated in Hermansky-Pudlak syndrome is a Rab32/38 guanine nucleotide exchange factor. *Curr. Biol.* **22**, 2135–2139 (2012).
40. Herrmann, E. et al. Structure of the metazoan Rab7 GEF complex Mon1-Ccz1-Bulli. *Proc. Natl. Acad. Sci. USA* **120**, e2301908120 (2023).
41. Onnis, A. et al. The small GTPase Rab29 is a common regulator of immune synapse assembly and ciliogenesis. *Cell Death Differ.* **22**, 1687–1699 (2015).
42. Sharma, R. et al. The CPLANE protein Fuzzy regulates ciliogenesis by suppressing actin polymerization at the base of the primary cilium via p190A RhoGAP. *Development* **151** https://doi.org/10.1242/dev.202322 (2024).
43. Yasunaga, T. et al. The polarity protein Inturned links NPHP4 to Daam1 to control the subapical actin network in multiciliated cells. *J. Cell Biol.* **211**, 963–973 (2015).
44. Megaw, R. et al. Ciliary tip actin dynamics regulate photoreceptor outer segment integrity. *Nat. Commun.* **15**, 4316 (2024).
45. Kohli, P. et al. The ciliary membrane-associated proteome reveals actin-binding proteins as key components of cilia. *EMBO Rep.* **18**, 1521–1535 (2017).
46. Schrauwen, I. et al. FAM92A underlies nonsyndromic postaxial polydactyly in humans and an abnormal limb and digit skeletal phenotype in mice. *J. Bone Min. Res.* **34**, 375–386 (2019).
47. Li, F. Q. et al. BAR domain-containing FAM92 proteins interact with Chibby1 to facilitate ciliogenesis. *Mol. Cell Biol.* **36**, 2668–2680 (2016).
48. Burke, M. C. et al. Chibby promotes ciliary vesicle formation and basal body docking during airway cell differentiation. *J. Cell Biol.* **207**, 123–137 (2014).
49. Wang, C. et al. Centrosomal protein Dzip1l binds Cby, promotes ciliary bud formation, and acts redundantly with Bromi to regulate ciliogenesis in the mouse. *Development* **145**, dev164236 (2018).
50. Lapart, J. A. et al. Dzip1 and Fam92 form a ciliary transition zone complex with cell type specific roles in Drosophila. *Elife* **8**, e49307 (2019).
51. Siller, S. S., Burke, M. C., Li, F. Q. & Takemaru, K. Chibby functions to preserve normal ciliary morphology through the regulation of intraflagellar transport in airway ciliated cells. *Cell Cycle* **14**, 3163–3172 (2015).
52. van Breugel, M., Rosa, E. S. I. & Andreeva, A. Structural validation and assessment of AlphaFold2 predictions for centrosomal and centriolar proteins and their complexes. *Commun. Biol.* **5**, 312 (2022).
53. Wang, L. et al. FAM92A1 is a BAR domain protein required for mitochondrial ultrastructure and function. *J. Cell Biol.* **218**, 97–111 (2019).
54. Evans, R. et al. Protein complex prediction with AlphaFold-Multimer. *bioRxiv*, 2021.2010.2004.463034 https://doi.org/10.1101/2021.10.04.463034 (2022).
55. Pylypenko, O., Hammich, H., Yu, I. M. & Houdusse, A. Rab GTPases and their interacting protein partners: Structural insights into Rab functional diversity. *Small GTPases* **9**, 22–48 (2018).
56. Ostermeier, C. & Brunger, A. T. Structural basis of Rab effector specificity: crystal structure of the small G protein Rab3A complexed with the effector domain of rabphilin-3A. *Cell* **96**, 363–374 (1999).
57. Chung, M. I. et al. Coordinated genomic control of ciliogenesis and cell movement by RFX2. *Elife* **3**, e01439 (2014).
58. Sang, L. et al. Mapping the NPHP-JBTS-MKS protein network reveals ciliopathy disease genes and pathways. *Cell* **145**, 513–528 (2011).
59. Zhao, H., Khan, Z. & Westlake, C. J. Ciliogenesis membrane dynamics and organization. *Semin Cell Dev. Biol.* **133**, 20–31 (2023).
60. Serres, M. P. et al. MiniBAR/GARRE1 is a dual Rac and Rab effector required for ciliogenesis. *Dev. Cell* **58**, 2477–2494.e2478 (2023).
61. Insinna, C. et al. Investigation of F-BAR domain PACSIN proteins uncovers membrane tubulation function in cilia assembly and transport. *Nat. Commun.* **10**, 428 (2019).
62. Sreekumar, V. & Norris, D. P. Cilia and development. *Curr. Opin. Genet. Dev.* **56**, 15–21 (2019).
63. Bruel, A. L. et al. Fifteen years of research on oral-facial-digital syndromes: from 1 to 16 causal genes. *J. Med. Genet.* **54**, 371–380 (2017).
64. Sobreira, N., Schiettecatte, F., Valle, D. & Hamosh, A. GeneMatcher: a matching tool for connecting investigators with an interest in the same gene. *Hum. Mutat.* **36**, 928–930 (2015).
65. Richards, S. et al. Standards and guidelines for the interpretation of sequence variants: a joint consensus recommendation of the American College of Medical Genetics and Genomics and the Association for Molecular Pathology. *Genet. Med.* **17**, 405–424 (2015).

66. Torres, J. Z., Miller, J. J. & Jackson, P. K. High-throughput generation of tagged stable cell lines for proteomic analysis. *Proteomics* **9**, 2888–2891 (2009).
67. Shevchenko, A., Tomas, H., Havlis, J., Olsen, J. V. & Mann, M. In-gel digestion for mass spectrometric characterization of proteins and proteomes. *Nat. Protoc.* **1**, 2856–2860 (2006).
68. Zybailov, B. et al. Statistical analysis of membrane proteome expression changes in Saccharomyces cerevisiae. *J. Proteome Res.* **5**, 2339–2347 (2006).
69. Ding, S. et al. Comparative Proteomics Reveals Strain-Specific β-TrCP Degradation via Rotavirus NSP1 Hijacking a Host Cullin-3-Rbx1 Complex. *PLoS Pathog.* **12**, e1005929 (2016).
70. Wood, C. W. et al. BAlaS: fast, interactive and accessible computational alanine-scanning using BudeAlaScan. *Bioinformatics* **36**, 2917–2919 (2020).

Acknowledgements

This work was supported by: The NICHD (R01HD085901) to E.M.M. and J.B.W; R01AR054396 and R01HD089918 to J.F.R.; R01GM121565, P01CA254867, R01DK127665 and R03TR004209 to P.K.J.; NIH R35GM122480 and the Welch Foundation (F-1515) to E.M.M.; Support from the Spanish Ministry of Science and Innovation (MICINN) through the program Juan de la Cierva to N.M.-G.; Swiss National Science Foundation (SNSF) grant number 32003B_219808 to I.F.; Support from Instituto de Salud Carlos III-FIS project PI22/00287, Xunta de Galicia (Centro de Investigación de Galicia CINBIO 2023-2027) Ref. ED431G-2023/06. To D.V.; An FPU predoctoral fellowship from the Spanish Ministry of Education, Culture and Sports (FPU 19/00175) to C. S.; and an ARCS Fellowship to C.D. KD is supported by National Institute of Child Health and Human Development (R00 HD092613) and BBSRC—National Science Foundation/Directorate for Biological Sciences [BB/X002179/1].

Author contributions

Neftalí Vazquez and Chanjae Lee conceived and directed the project, performed *Xenopus* experiments, and helped assemble the manuscript. Irene Valenzuela conceived and directed the project, performed human clinical assessment and genetics, and helped assemble the manuscript. Marcelo Chávez, Nancie A. Mooney, Janos Demeter performed proteomic analysis. Michinori Toriyama, Krishna Vaidyanathan performed *Xenopus* experiments. Tynan P. Gardner and Kevin Drew performed protein structure predictions. Thao P. Phan, Camille Derderian, Elle C. Roberson performed experiments with mammalian cell culture. Mohammad Ovais Aziz-Zanjani, Ivon Cusco, Marta Codina, Núria Martínez-Gil, Diana Valverde, Carlos Solarat, Ange-Line Buel, Cristel Thauvin-Robinet, Elisabeth Steichen, Isabel Filges, Pascal Joset, Julie De Geyter performed human clinical assessment and genetics. Edward M. Marcotte, Peter K. Jackson, and Jeremy F. Reiter designed and supervised elements of the project. Eduardo F. Tizzano and John B. Wallingford conceived and directed the project and assembled the manuscript.

Competing interests

The authors declare no competing interests.

Additional information

Supplementary information The online version contains supplementary material available at https://doi.org/10.1038/s41467-025-61005-8.

Correspondence and requests for materials should be addressed to Eduardo F. Tizzano or John B. Wallingford.

Peer review information *Nature Communications* thanks the anonymous reviewers for their contribution to the peer review of this work. A peer review file is available.

Reprints and permissions information is available at http://www.nature.com/reprints

Publisher's note Springer Nature remains neutral with regard to jurisdictional claims in published maps and institutional affiliations.

[1]Department of Molecular Biosciences, University of Texas at Austin, Austin, TX, USA. [2]Department of Clinical and Molecular Genetics, Vall d´Hebron University Hospital. European Reference Network on Rare Congenital Malformations and Rare Intellectual Disability (ERN-ITHACA), Medicine Genetics Group, Vall d´Hebron Research Institute, Barcelona, Spain. [3]Department of Biochemistry and Biophysics, Cardiovascular Research Institute, University of California, San Francisco, San Francisco, CA, USA. [4]Baxter Laboratory, Department of Microbiology & Immunology, Stanford University School of Medicine, Stanford, CA, USA. [5]CINBIO, University of Vigo and Research Group on Rare Diseases and Pediatric Medicine, Health Research Institute Galicia Sur (IIS Galicia Sur), SERGASUVIGO, Vigo, Spain. [6]Functional Unity of Innovative Diagnosis for Rare Diseases and Inserm UMR1231 team GAD, University of Burgundy, Dijon, France. [7]Department of Pediatrics, Medical School, University of Innsbruck, Innsbruck, Austria. [8]Medical Genetics, Institute of Medical Genetics and Pathology and Department of Clinical Research, University Hospital Basel, Basel, Switzerland. [9]Department of Biomedical Sciences, School of Biological and Environmental Sciences, Kwansei Gakuin University, Sanda, Hyogo, Japan. [10]Department of Biological Sciences, University of Illinois at Chicago, Chicago, IL, USA. [11]Developmental Biology and Pediatrics, CU Anschutz Medical Campus, Aurora, CO, USA. [12]These authors contributed equally: Neftalí Vazquez, Chanjae Lee, Irene Valenzuela, Eduardo F. Tizzano, John B. Wallingford. ✉e-mail: eduardo.tizzano@vallhebron.cat; wallingford@utexas.edu